Petroleum Science 21 (2024) 3079–3089

Contents lists available at ScienceDirect

Petroleum Science

journal homepage: www.keaipublishing.com/en/journals/petroleum-science

Original Paper

Efficient anti-aliasing and anti-leakage Fourier transform for high-dimensional seismic data regularization using cube removal and GPU

Lu Liu [a, *], Sindi Ghada [b], Fu-Hao Qin [c], Youngseo Kim [c], Vladimir Aleksic [d], Hong-Wei Liu [e]

[a] Aramco Research Center - Beijing, Aramco Asia, Beijing, 100102, China
[b] KAUST Research Center Group, Saudi Aramco, Thuwal, 23955-6900, Saudi Arabia
[c] EXPEC Advanced Research Center, Saudi Aramco, Dhahran, 31311, Saudi Arabia
[d] Geophysical Imaging Department, Saudi Aramco, Dhahran, 31311, Saudi Arabia
[e] National Key Laboratory of Deep Oil and Gas, China University of Petroleum (East China), Qingdao, 266580, Shandong, China

ARTICLE INFO

Article history:
Received 7 November 2023
Received in revised form
4 January 2024
Accepted 1 April 2024
Available online 4 April 2024

Edited by Meng-Jiao Zhou

Keywords:
High-dimensional regularization
GPU
Anti-aliasing
Anti-leakage

ABSTRACT

Seismic data is commonly acquired sparsely and irregularly, which necessitates the regularization of seismic data with anti-aliasing and anti-leakage methods during seismic data processing. We propose a novel method of 4D anti-aliasing and anti-leakage Fourier transform using a cube-removal strategy to address the combination of irregular sampling and aliasing in high-dimensional seismic data. We compute a weighting function by stacking the spectrum along the radial lines, apply this function to suppress the aliasing energy, and then iteratively pick the dominant amplitude cube to construct the Fourier spectrum. The proposed method is very efficient due to a cube removal strategy for accelerating the convergence of Fourier reconstruction and a well-designed parallel architecture using CPU/GPU collaborative computing. To better fill the acquisition holes from 5D seismic data and meanwhile considering the GPU memory limitation, we developed the anti-aliasing and anti-leakage Fourier transform method in 4D with the remaining spatial dimension looped. The entire workflow is composed of three steps: data splitting, 4D regularization, and data merging. Numerical tests on both synthetic and field data examples demonstrate the high efficiency and effectiveness of our approach.

1. Introduction

Regularly and densely sampled seismic data can benefit various seismic processing methodologies within the realm of geophysical exploration. This includes data-driven multiple elimination (Verschuur et al., 1992), plane-wave gathers (Liu et al., 2018), seismic migration (Etgen et al., 2009; Liu, 2019), surface-noise removal (Qin et al., 2012), and amplitude variation with azimuth or offset analyses (Almutlaq and Margrave, 2010). Obviously, directly acquiring more data is the best way to obtain 3D regularly sampled data; however, this is prohibitively expensive and even impossible in many cases due to complex topography, cable feathering, and necessity for bad traces editing. Therefore, seismic data regularization or interpolation becomes pivotal in overcoming these limitations.

In the past, data regularization or interpolation was predominantly conducted in low-dimensional space. However, a higher-dimensional (>3D) methods can provide more data from different spatial dimensions and thus lead to an enhanced outcomes (Jin, 2010; Xu et al., 2010). For this reason, the development of high-dimensional seismic data regularization approaches is deemed essential.

Aliasing and spectral leakage represent primary artifacts during seismic data processing and present challenges in data regularization. Consequently, various methods have been proposed over recent decades to tackle these artifacts. Examples include, but are not limited to, transform-based data regularization (Hindriks and Duijndam, 2000; Zwartjes and Gisolf, 2007), convolution-based methods (Spitz, 1991; Crawley, 2001), wavefields continuation operator method (Zwartjes and Gisolf, 2007), minimum weighted norm inversion (Liu and Sacchi, 2004), deep learning strategies (Wang et al., 2019, 2023), projection onto convex sets (Abma and Kabir, 2006), and antileakage Fourier transform (ALFT) (Xu et al., 2005, 2010; Qin et al., 2018).

* Corresponding author.
E-mail address: lu.liu@aramcoasia.com (L. Liu).

https://doi.org/10.1016/j.petsci.2024.04.002

Transform-based seismic data regularization typically coverts the non-uniform data into another domain using Fourier transform (Duijndam et al., 1999; Zwartjes and Sacchi, 2007), Radon transform (Trad et al., 2002), or wavelet transform (Pawelec et al., 2019). It then estimates the corresponding coefficients through least-square sparse inversion, and finally outputs the uniform data by the associated inverse transform. For example, Duijndam et al. (1999) proposed the Fourier-domain reconstruction method to interpolate non-uniformly sampled data by assuming band-limited input. Zwartjes and Sacchi (2007) further developed this method to non-uniformly sampled and aliased data using Fourier-domain sparse inversion and a weighting function from the non-aliased part of the spectrum.

Convolution-based methods operate under the assumption that the regularized seismic data can be expressed as a convolution between the input data and a given function (like sinc-function interpolation) or a series of coefficients to be solved. Prediction error filters (PEFs) represent a commonly employed technique within this category. Spitz (1991) predicted the linear events for aliased seismic data by assuming that the data are stationary and regular. Crawley (2001) further proposed nonstationary PEFs to solve the interpolation of curved events.

Wavefields continuation operator techniques involve applying a forward operator to non-uniform seismic data and obtain the associated model, based on which an inverse operator is followed to produce the missing offsets and azimuths. Such operators can be dip moveout (DMO), azimuth moveout (Chemingui, 1999), or migration (Verma et al., 2016), etc. This category of approaches can preserve lateral discontinuities, but may introduce unavoidable artifacts in a complex geological structure due to depending on the velocity model. Moreover, the integral of coarsely sampled data from the wavefields continuation operator also results in artifacts. Inversion strategy can ameliorate the results but greatly increase the computational cost (Nemeth et al., 1999).

The minimum weighted norm inversion method is efficient due to the applied fast Fourier transform (FFT); however, it requires data binning to regularize the spatial positions, potentially causing data distortion. Deep learning techniques establish an abstract relation between the sparse input data and desired regularized data through extensive training datasets. Once this relation is well established, the forward prediction can be exceptionally efficient. However, this procedure usually requires one robust deterministic method for labeling the training samples (Zhang et al., 2020). Some self-supervised learning approaches have been proposed in recent years to overcome the limitation of labeling, but compromise the prediction accuracy (Fang et al., 2023). Projection onto convex sets is a popular and computationally efficient method but requires an appropriate selection of a robust threshold, which can be difficult to determine.

The ALFT methods iteratively construct the Fourier coefficients by searching for the element with maximum amplitude and subtracting the associated components from the original data until all the significant Fourier coefficients are estimated (Xu et al., 2005). ALFT is theoretically straightforward and robust to implement and hence attracts considerable studies. For example, Schonewille et al. (2009) improved the ALFT by estimating a weighting function from the low-frequency data and applying to high-frequency data to help event picking; Ebrahim et al. (2018) introduced antileakage scheme to least-squares spectral analysis to attenuate the spectral leakage and consequently regularize irregular data series. However, ALFT tends to incur significant computational cost in high dimension (Xu et al., 2010; Whiteside et al., 2014).

To alleviate computational issues for high-dimensional seismic data regularization using ALFT, we proposed employing 4D ALFT, speeding up the conventional ALFT workflow by cube removal, and designing a CPU/GPU collaborative computing strategy. To guarantee the events linearity and reduce the memory cost, the high-dimensional ALFT is usually implemented using a windowing strategy with sufficient overlapping and tapering. However, the problem of spatial aliasing may occur more likely within the windows. Therefore, anti-aliasing scheme is also required within ALFT to improve the regularization results (Schonewille et al., 2009; Yang et al., 2017).

We organized the paper as follows. We demonstrated the principle of 4D anti-aliasing and anti-leakage seismic data regularization, illustrate the cube-removal-based workflow, discuss the CPU/GPU collaborative parallel computing, and finally validate our method on both synthetic and field datasets.

2. Method

2.1. Anti-leakage fourier transform

Suppose that $d(x_n, t)$ are seismic data with N traces non-uniformly sampled at locations $[x_0, x_1 \ldots x_{N-1}]$ in the ascending order, and the associated Fourier coefficients in the frequency-wavenumber domain can be computed via nonuniform discrete Fourier transform (NDFT),

$$D(m\Delta k, \omega) = \sum_{n=0}^{N-1} d(x_n, \omega) \mathrm{e}^{im\Delta k x_n} \Delta x_n, \tag{1}$$

where $\Delta k = 2\pi/(x_{N-1} - x_0)$, m is the wavenumber index, and Δx_n represents the distance between two consecutive traces. $D(m\Delta k, \omega)$ can be expressed as a convolution between a point-spread function and a spectrum from the corresponding uniformly sampled signals (Zwartjes and Sacchi, 2007), and is contaminated by spectrum leakage.

To mitigate these leakages, Xu et al. (2005) proposed the ALFT regularization, which contains the following steps.

1) Compute frequency-wavenumber-domain wavefields $D(m\Delta k, \omega)$ using Eq. (1).
2) Select and output the strongest Fourier component for each frequency slice.
3) Subtract the contribution of this strongest component and update the Fourier components via

$$D_{\text{update}}(m\Delta k, \omega) = D(m\Delta k, \omega) - \sum_{n=0}^{N-1} D(m\Delta k, \omega) \mathrm{e}^{i(m\Delta k - k_{\max})x_n} \Delta x_n, \tag{2}$$

4) Input the updated Fourier components into step 2 until the data residual is small enough or reaches the user-given picks number.
5) Create the regularized seismic data by applying inverse FFT to the estimated spectrum.

Many publications have showcased the efficacy of ALFT regularization in handling nonuniformly sampled seismic data. However, its performance may degrade for very sparse data where aliasing happens, especially for seismic data in crossline direction that are generally aliased in the cases of complex geologic structures. On the other hand, the computational cost, determined by the volume of wavenumbers and input traces across all dimensions, dramatically increases for the high-dimensional ALFT regularization. In the following sections, we will discuss how to resolve the spectral leakage and aliasing simultaneously and accelerate high-dimensional ALFT regularization significantly.

2.2. Anti-aliasing ALFT

The above ALFT workflow functions nicely if the strongest amplitude element is always the $f-k$ response of a real event. However, scenarios exist where this element is an artifact caused by noisy input data, or wraparound of an aliased event, or energy leakage from another event. Fig. 1 demonstrates one of these cases with an example of crossing linear events, showing the effect of spatial sampling on the Fourier spectrum. Fig. 1(a) shows the densely and uniformly sampled data and the corresponding $f-k$ spectrum in Fig. 1(b) are free of spectral leakage and aliasing. Fig. 1(c) shows the aliased data, obtained by uniformly extracting one-eighth traces from Fig. 1(a). Its $f-k$ spectrum in Fig. 1(d) shows periodic aliases but without spectral leakage. We then randomly drop 30% of the traces to generate Fig. 1(e), and the spectrum in Fig. 1(f) shows aliasing as well as artifacts (dashed red ellipse) from sampling irregularities. Fig. 1(f) is the case we usually need to handle in practice, where the ALFT method may select aliased components rather than the true components, meaning the events are not well reconstructed at new locations.

We then augmented the ALFT regularization method by incorporating a robust anti-aliasing capability through the computation of an appropriated weighting function aimed at mitigating the aliased energy prior to maximum energy selection. In $f-k$ domain, the dip of a linear event can be expressed by $p = k/\omega$, and the true signals share a common origin at $(\omega = 0, k = 0)$, whereas the aliasing lacks this commonality. This favorable property enables us to design an anti-aliasing approach.

Assuming that the events are approximately linear within a high-dimensional window, we can compute the weighting function $W(k', \omega')$ by stacking the $f-k$ spectrum along the radiating lines, and the equation is written as

$$W(k', \omega') = \sum_{\omega} |D(k'\omega \,/\, \omega', \omega)|, \tag{3}$$

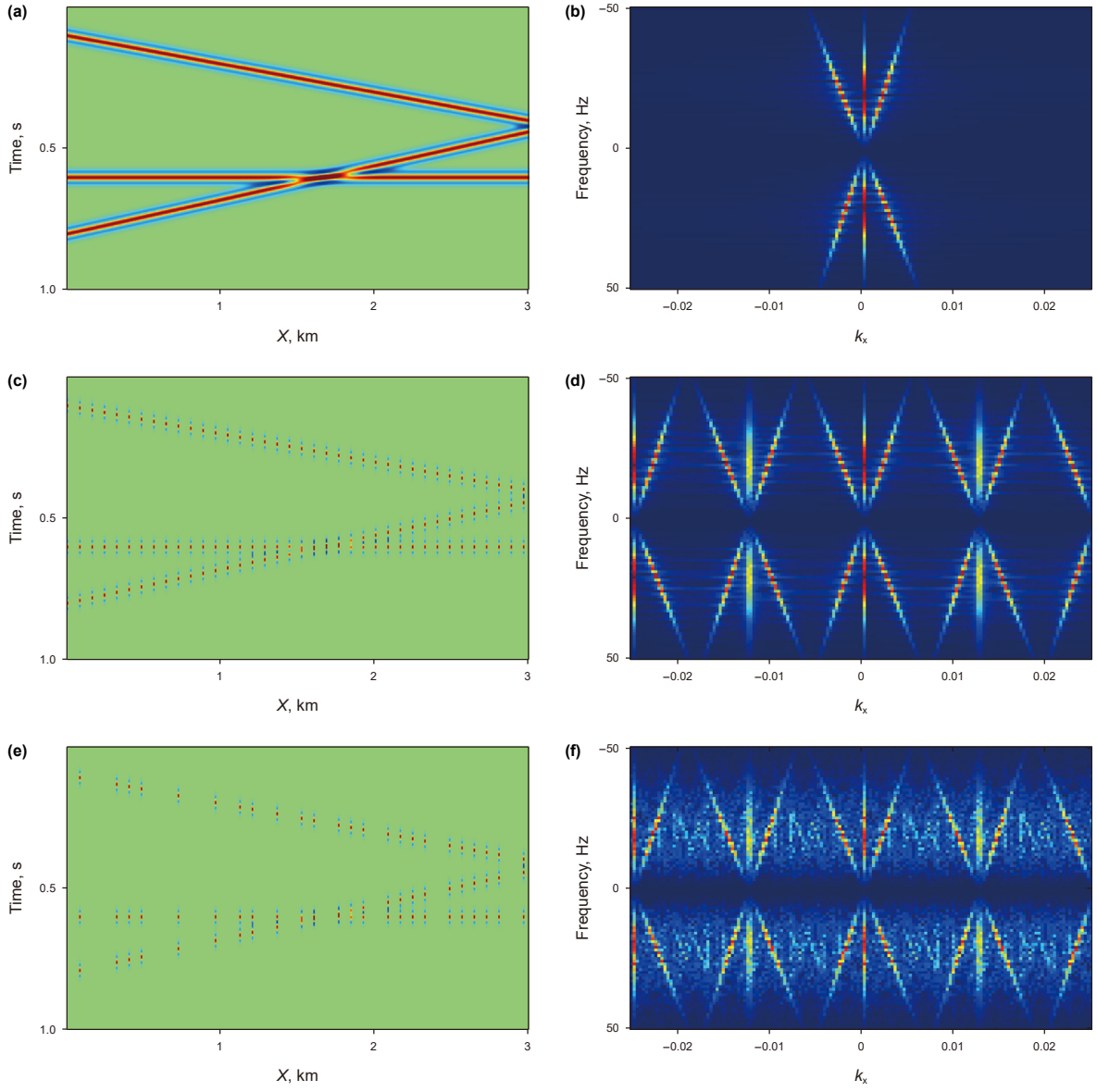

Fig. 1. An example of aliasing and spectral leakage, including **(a)** the dense and uniformly acquired data and **(b)** the associated $f-k$ spectrum, **(c)** the sparse and uniformly acquired data and **(d)** the associated $f-k$ spectrum, **(e)** the sparse data with 30% traces missing and **(f)** associated $f-k$ spectrum. The red ellipse marks the spectral leakage.

where k' and ω' are the wavenumber and frequency indices for the weighting matrix or the center of the integral window, and ω indicates the frequency in the original spectrum used for integral (Schonewille et al., 2009; Qin et al., 2012). A typical integral range of ω is 5–10 Hz. Leveraging the fact that the $f-k$ responses of linear events are radial lines emanating from the origin ($\omega = 0, k = 0$), Eq. (3) can enhance the true signals while dampening the aliasing that does not point to the origin. Fig. 2(a) shows the weights for the spectrum in Fig. 1(f) using Eq. (3) and integral range of 10 Hz, revealing that the true Fourier components corresponds to high weights whereas the aliasing exhibits considerably low weights. The weighting function is then applied to the $f-k$ spectrum before selecting the maximum energy. The result in Fig. 2(b) clearly highlights the true Fourier components and effectively suppresses the aliasing. The evident disparity in energy between the true components and the aliasing is sufficient to avoid picking the aliasing as the maximum component. The workflow for anti-aliasing ALFT regularization is discussed in the subsequent section.

2.3. Cube-removal scheme

The high computational cost for high-dimensional ALFT regularization hinders its widespread application (Whiteside et al., 2014). We introduced a spectral cube-removal technique to speed up the method. The cube removal scheme assumes that the points adjacent to the point with maximum energy also has strong energy, and thus we can subtract the contribution of a cube for one iteration, rather than a single point. This can dramatically decrease the implementation of maximum energy searching and weighting function computing.

The whole workflow of the anti-aliasing ALFT regularization using cube removal is:

1) Compute the $f-k$ spectrum of the seismic data using Eq. (1).
2) Estimate the weighting function using Eq. (3) and apply to the $f-k$ spectrum.
3) Find the element with maximum energy for each frequency slice.
4) Output the $3 \times 3 \times 3$ cube centered on this selected point. Loop over each position within this cube, output the corresponding element from the input spectrum to the estimated aliasing- and leakage-free spectrum, and then update the input spectrum using Eq. (2). Continue the loop until all the element within the cube is processed.
5) Repeat step 2 to 4 until the data residual is small enough or reaching the user-given picks number.
6) Output the regularized seismic data using inversion FFT.

We then used a simple example to validate our proposed cube-removal anti-aliasing ALFT. We prepared a 4D matrix $d(t, x, y, z)$ as the true data whose spatial grid numbers are $25 \times 37 \times 25$ (corresponding x, y, and z spatial dimension, respectively). The spatial intervals for the three dimensions are all 15 m and the recording length is 2 s. We use two 3D displays to depict this 4D data. Fig. 3(a) and (b) both show a 3D matrix, corresponding to data $d(t, y, z; x = 225\ \text{m})$ and $d(t,\ x,\ z; y =\ 225\ \text{m})$, respectively. We randomly selected 1500 traces (about 6.5 % of the original dense traces) as the input for data regularization, shown in Fig. 3(c) and (d). The input traces are clearly sparse and nonuniform, resulting in severe aliasing and leakage. To validate that, we compute the Fourier spectra for the sparse data (Fig. 3(c)) and true data (Fig. 3(a)), shown in Fig. 4. Compared to the Fourier spectrum of the true data (Fig. 4(a)), the spectrum of input data (Fig. 4(b)) is strongly distorted by aliasing and spectral leakage. We then apply the cube-removal anti-aliasing ALFT method to reconstruct the data with 80 iterations, and the results in Fig. 3(e) and (f) successfully recover the missing data. Therefore, the weighting function well suppresses the aliasing, further leading to correct selections of the maximum elements in the presence of aliasing. We next discussed how the cube-removal scheme can improve efficiency.

To demonstrate the efficiency of the cube-removal method, we re-implemented the regularization using the point-removal 4D anti-aliasing ALFT method, which means we only output one point in step 4 of the above workflow as the way a classic ALFT method (Xu et al., 2005) implements. The input data and the parameters are the same as the test in Fig. 3, and the results after 80 iterations are in Fig. 5. It shows that the events are also well recovered, while some areas, for example the one indicated by the black arrow, have unfocused leaked energy that deviates from the true data in Fig. 3(b). Note that the point-removal result can be ameliorated by increasing the iterations, as our trial results suggest. In other words, the associated cube-removal result in Fig. 3(e) and (f) outperforms the single-removal one for relatively few iterations.

We further compared the error value over iterations between the cube-removal and point-removal scheme, shown in Fig. 6. The error is defined as the L2 norm of the difference between the 4D regularized and true data. Conclusions can be drawn that the cube-removal method converges fast. Despite the fact that one iteration of the cube-removal method costs slightly more than point

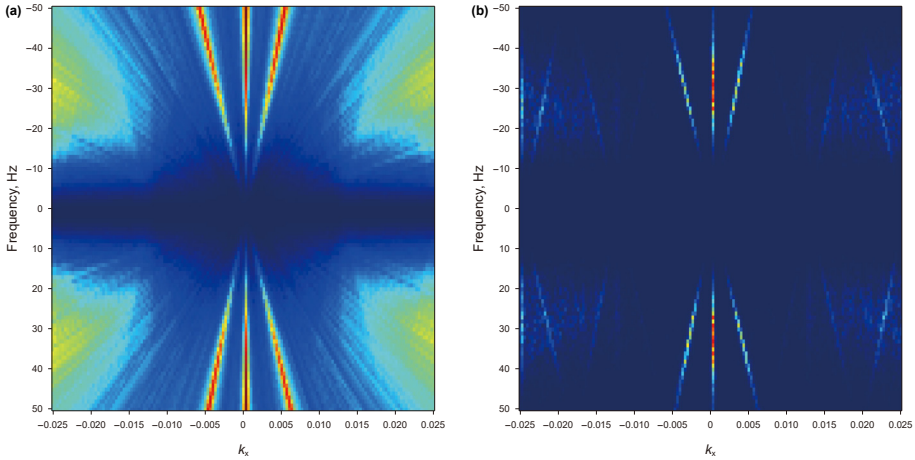

Fig. 2. **(a)** Weighting function for the data in Fig. 1(f) and **(b)** the associated weighted $f-k$ spectrum.

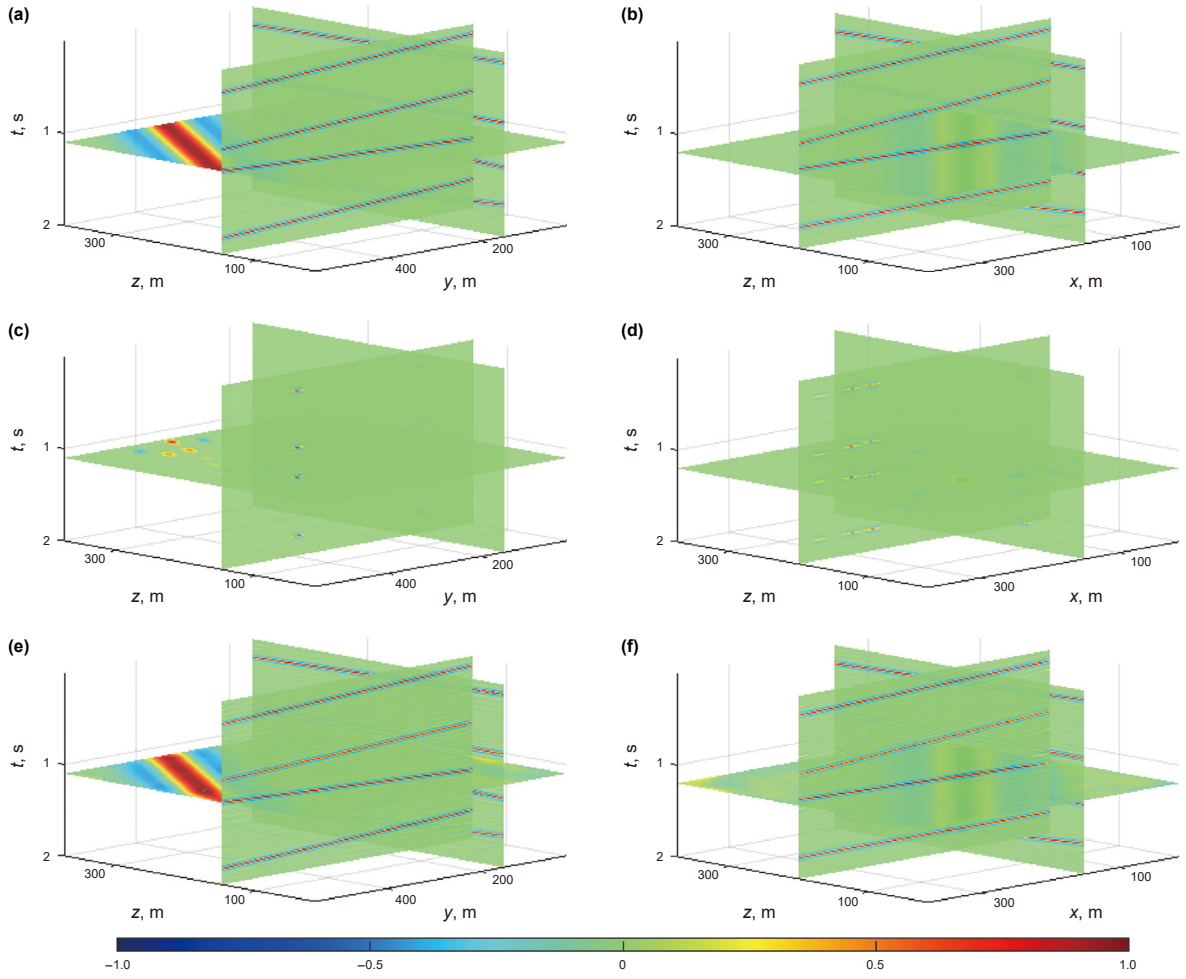

Fig. 3. Result of 4D ALFT including **(a)** true data $d(t,y,z;x=225\ \mathrm{m})$ and **(b)** $d(t,x,z;y=225\ \mathrm{m})$, sparse input data corresponding to **(c)** $d(t,y,z;x=225\ \mathrm{m})$ and **(d)** $d(t,x,z;y=225\ \mathrm{m})$, the regularized result using cube-remove 4D anti-aliasing ALFT method corresponding to **(e)** $d(t,y,z;x=225\ \mathrm{m})$ and **(f)** $d(t,x,z;y=225\ \mathrm{m})$. All the subfigures are drawn using the same color bar.

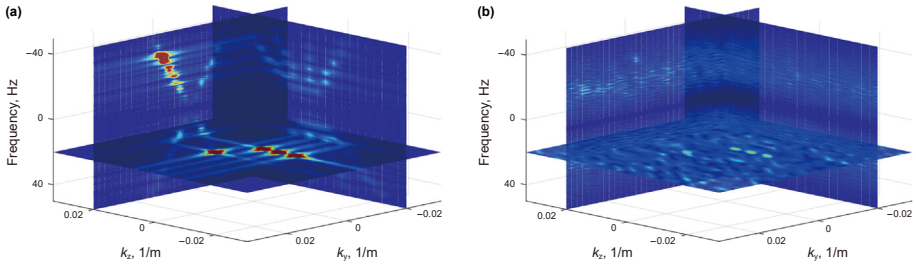

Fig. 4. The $f-k$ spectrum for **(a)** true data $d(t,y,z;x=225\ \mathrm{m})$ and **(b)** the corresponding sparse input data.

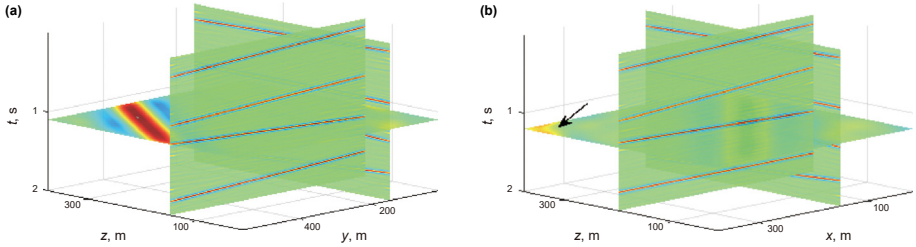

Fig. 5. The regularized result using the point-removal 4D anti-aliasing ALFT method corresponding to **(a)** $d(t,y,z;x=225\ \mathrm{m})$ and **(b)** $d(t,x,z;y=225\ \mathrm{m})$. The number of picks is 80, same as the test in Fig. 3. The arrow marks the area which is inconsistent with the true data.

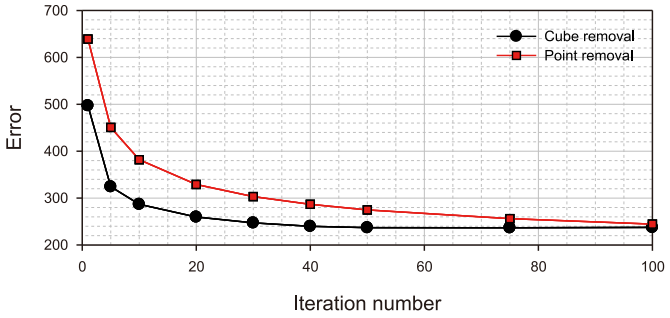

Fig. 6. The comparison of errors over iterations between point-removal and cube-removal 4D anti-aliasing ALFT method.

removal, the whole cost still dramatically lower. In this example, cube removal uses 4.2 s for 40 iterations to achieve an almost equivalent error with point removal, which takes 6.1 s for 100 iterations. Therefore, this example demonstrate that compared to the cube-removal scheme, the point-removal scheme requires an additional 50% computational time to achieve a comparable outcome.

2.4. CPU/GPU collaborative computing

To further boost the efficiency, we designed a multi-level parallel architecture via CPU/GPU collaborative parallel computing (Liu et al., 2015). This architecture is composed of message passing interface (MPI), multiple GPU devices, and GPU fine-grained parallel computing. Fig. 7 shows the master-slave parallel architecture of 4D ALFT regularization. The master processor coordinates tasks by reading the spatial locations from the headers and assigning tasks to slave processors. Each slave processor is connected with one GPU device, splitting the whole 5D seismic data into numerous 4D segments. These segments are read from the disk based on the range that master processor defines and then sent to GPUs for regularization. The only interaction between the master and slave computations is that the master starts the slave computations by sending the window index, and the slaves request unprocessed windows after writing the regularized data. After that, we apply a parallel merging to combine the data from numerous 4D windows to the complete 5D dataset. Note that the data compression technique can be used to compress the regularized result from each 4D window, and then the compressed data that is much smaller than the original one is read and decompressed for merging. The compression ratio is dependent on the accuracy of the decompressed data (NVIDIA Corporation, 2022). To summarize, the proposed parallel architecture has the features of parallel data splitting and merging, on-the-fly splitting, and high-efficiency multi-GPUs regularization.

To evaluate the efficiency of the GPU kernels, we prepared one 4D seismic data with maximum recording time of 8 s for a small spatial window ($65 \times 81 \times 81$). We then use one GPU device of Quadro RTX 6000 to process this data, meanwhile use the CPU version and same parameters to reprocess this data on an Intel Xeon CPU running at 2.20 GHz with 48 processors. Note that the CPU version has OpenMP parallel computing applied over the time window loop, meaning that we are comparing the GPU kernels with OpenMP parallel CPU version. The efficiency comparison between CPU and GPU version is shown in Fig. 8(a). It demonstrates that the GPU kernels achieve high acceleration ratios of 163, 85, 32, and 15, compared with the CPU version for different time windows, respectively. It is worth mentioning that the time window cannot

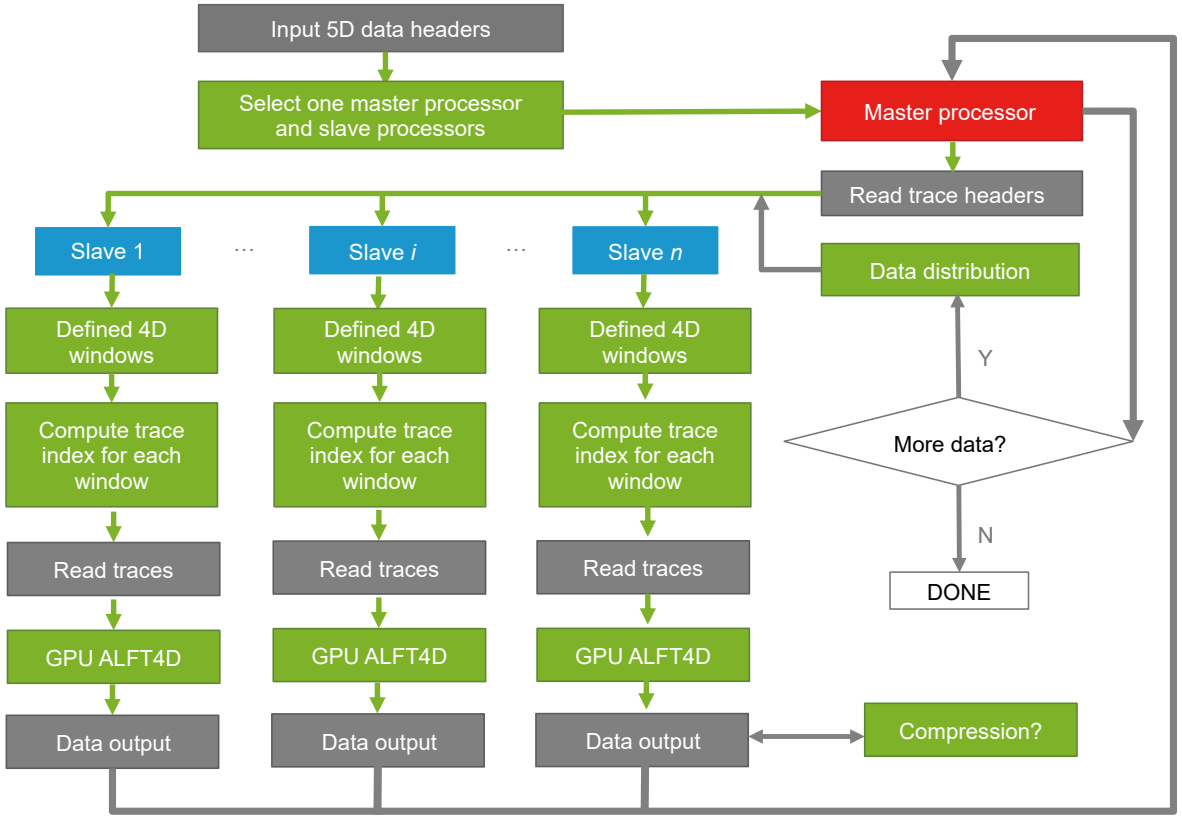

Fig. 7. The parallel architecture of 4D ALFT regularization. Blue, green, grey, and red rectangles represent slave, computation, data I/O, and master, respectively.

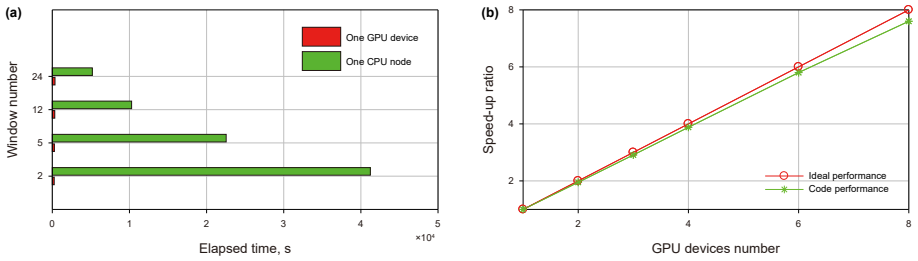

Fig. 8. Code performance of 4D ALFT regularization including **(a)** the efficiency comparison between the GPU and CPU version and **(b)** the scalability performance.

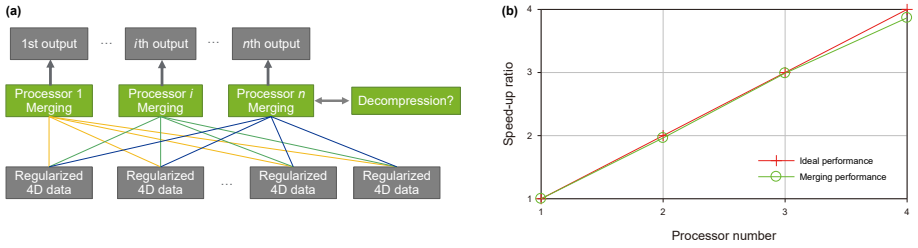

Fig. 9. **(a)** The parallel architecture of seismic data merging and **(b)** the associated scalability performance.

be too small, otherwise the windowed data is unable to capture the linearity of the seismic events. A typical time window length ranges from 500 to 2000 ms. Additionally, we also assessed the performance scalability of the parallel architecture (Fig. 7) with respect to the number of GPU devices. The result in Fig. 8(b) clearly shows that the ALFT method can achieve nearly linear performance scalability.

The merging procedure involves going through each output index and computing the associated window that contribute to this location. This computation is realized by scanning the window boundary from all the windows, followed by merging all the related windowed regularized data using a weighted stacking and writing a group of traces along the fast spatial dimension onto the disk. If the windowed data are compressed in the regularization procedure, the data require decompression before merging. The merging procedure is accelerated by MPI parallel computing, which is applied over the two slowest spatial dimensions. The number of the output files corresponds to the number of processors employed for merging. The above procedure is further illustrated in Fig. 9(a). Furthermore, the scalability test depicted in Fig. 9(b) affirms that this parallel merging exhibits a linear acceleration ratio concerning the processors number.

3. Results

In this section, we applied the 4D cube-removal anti-aliasing ALFT regularization to both synthetic and field data sets and validate the regularization results by depth migration or NMO stacking.

3.1. Application to synthetic data set

Here we applyed our method to a 3D synthetic dataset generated from a partial 3D SEAM Arid model (2.25 km × 6 km × 3 km) presented in Fig. 10. We used a Ricker wavelet with a peak frequency of 20 Hz to generate 1280 common-shot gathers via 3D acoustic finite-difference modeling. The 3D survey encompasses 40 source lines with randomly spaced line intervals ranging from 120 to 180 m. The source interval along crossline direction is randomly selected from 60 to 120 m, leading irregular and sparse source locations shown in Fig. 11(a). The 67 receiver lines are uniformly distributed on the surface with 15 m interval for the inline direction and 60 m interval in the crossline direction. We then randomly dropped 75% of the input traces. The missing traces and randomly placed sources create sparse and irregular acquisition geometry that requires the high-dimensional ALFT to reconstruct the seismic data. The maximum offset is 6 km and the maximum recording time is 2.5 s with 1 ms time-sampling interval.

The source locations are regularized using a grid size of 75 m × 90 m, and the receiver interval for inline and crossline direction after regularization is 15 and 60 m, respectively. Fig. 11(b) shows the regularized source locations, which achieves a dense and regular sampling acquisition geometry. Besides, the seismic data are reasonably reconstructed. For instance, the shot gathers presented in Fig. 12(a) and (c) exhibit severe irregularity and sparsity, with traces in some areas being entirely absent (marked by the red arrow), making seismic events identification challenging. However, the regularized results depicted in Fig. 12(b) and (d) recover all the traces and present a substantial improvement in the continuity of seismic reflections compared to the input data.

To validate the regularized results, we randomly selected one trace from the original input data of Fig. 12(c) and compared it with the corresponding reconstructed trace from Fig. 12(d). The comparison in Fig. 13 indicates that the regularized trace preserves the

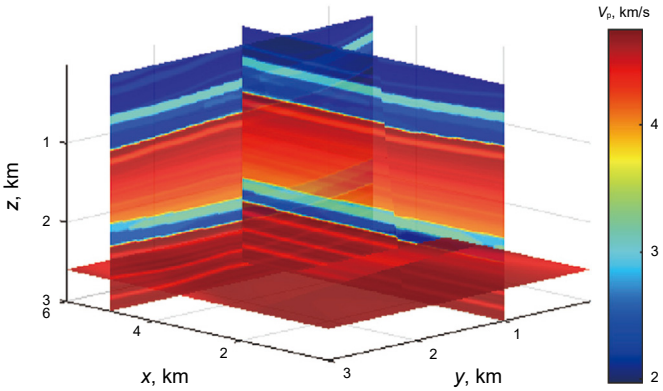

Fig. 10. The true velocity model for the synthetic data test.

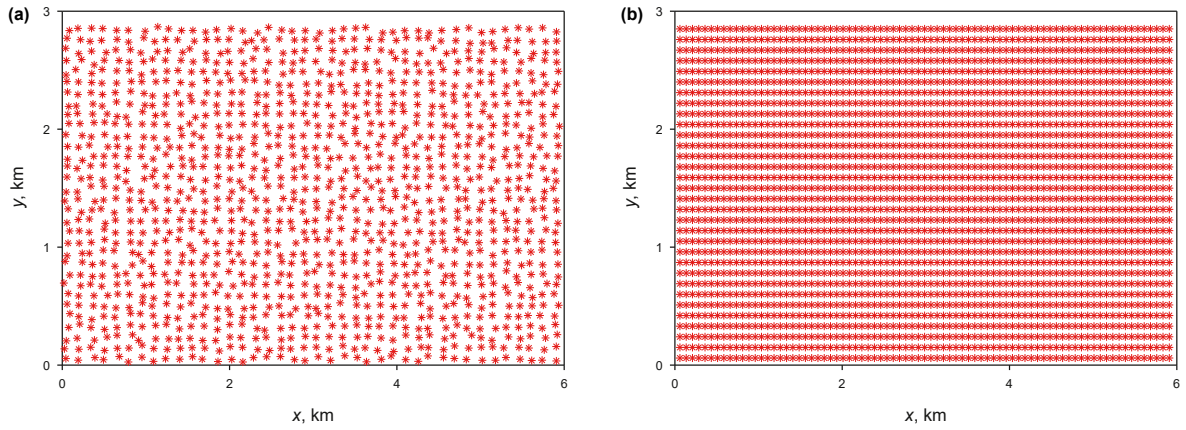

Fig. 11. Source locations (**a**) before and (**b**) after our method.

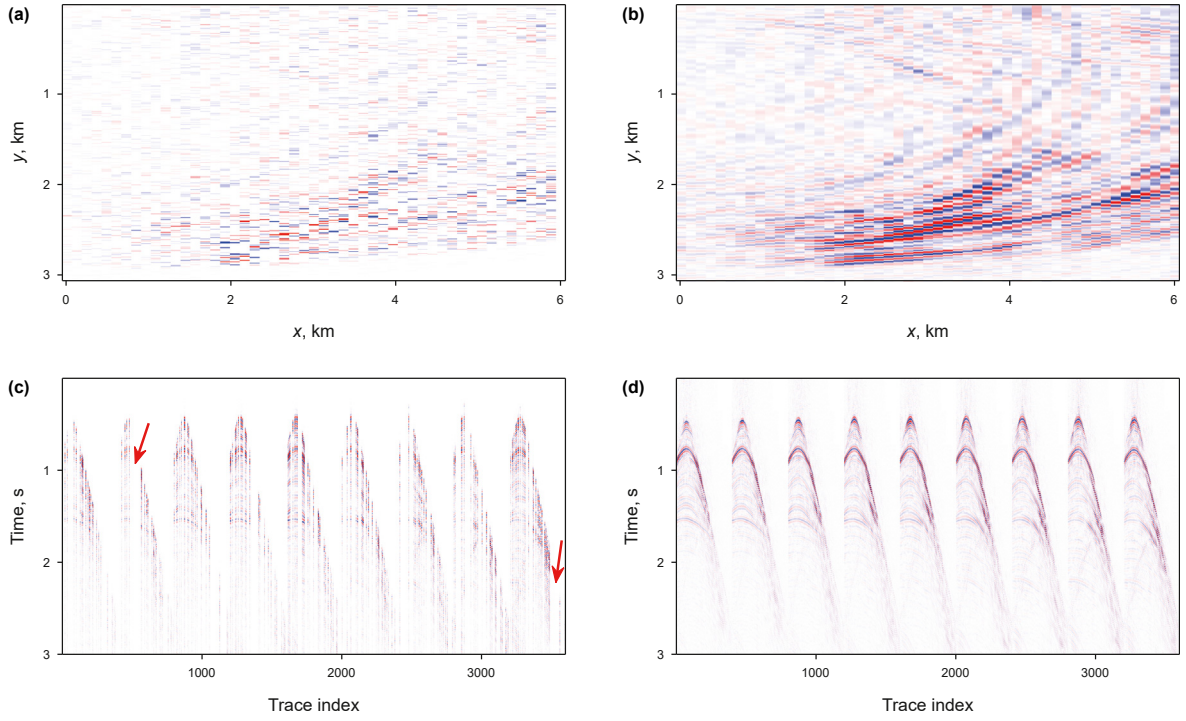

Fig. 12. Shot gathers comparison including (**a**) the time slice of the input shot gather at 2.5 s and (**b**) the associated regularized result, as well as (**c**) partial shot gathers before and (**d**) after regularization. The red arrows mark the acquisition gaps.

amplitude and phase of the original trace. The minor amplitude discrepancy can be reduced by increasing the number of iterations, as the method selects the elements based on energy. Additionally, we compare the $f-k$ spectra for the shot gathers in Fig. 14, showing the aliasing and leakage in the original input data marked by the red arrow in Fig. 14(a) are effectively suppressed by our method, compared to the spectrum of the regularized data in Fig. 14(b).

We applied the reverse-time migration (RTM) to both the input and the regularized data and displayed the associated images in Fig. 15. The image events from the regularized data exhibit enhanced coherence, focus, and fewer artifacts compared to those from the input data, such as the regions indicated by the dashed black rectangles.

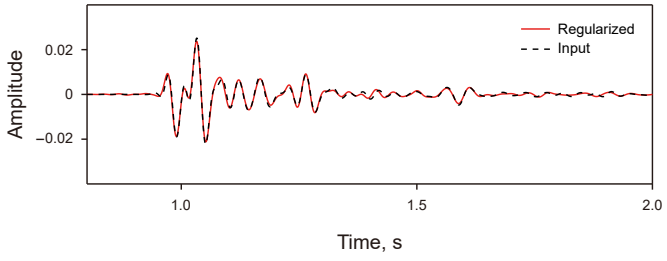

Fig. 13. Trace comparison between the regularized data (solid red line) and the input data (dashed black line).

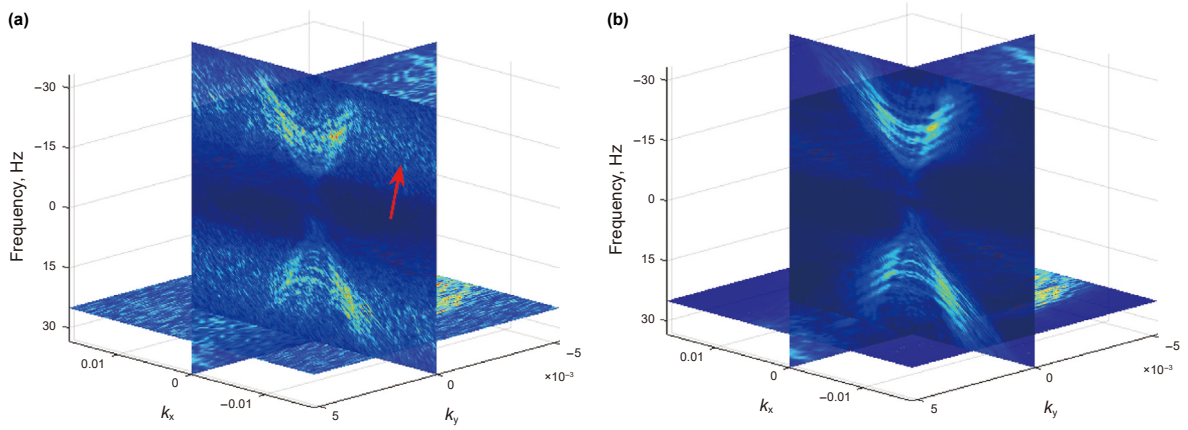

Fig. 14. The $f-k$ spectrum for **(a)** the input shot gather in Fig. 12(c) and **(b)** the corresponding reconstructed data.

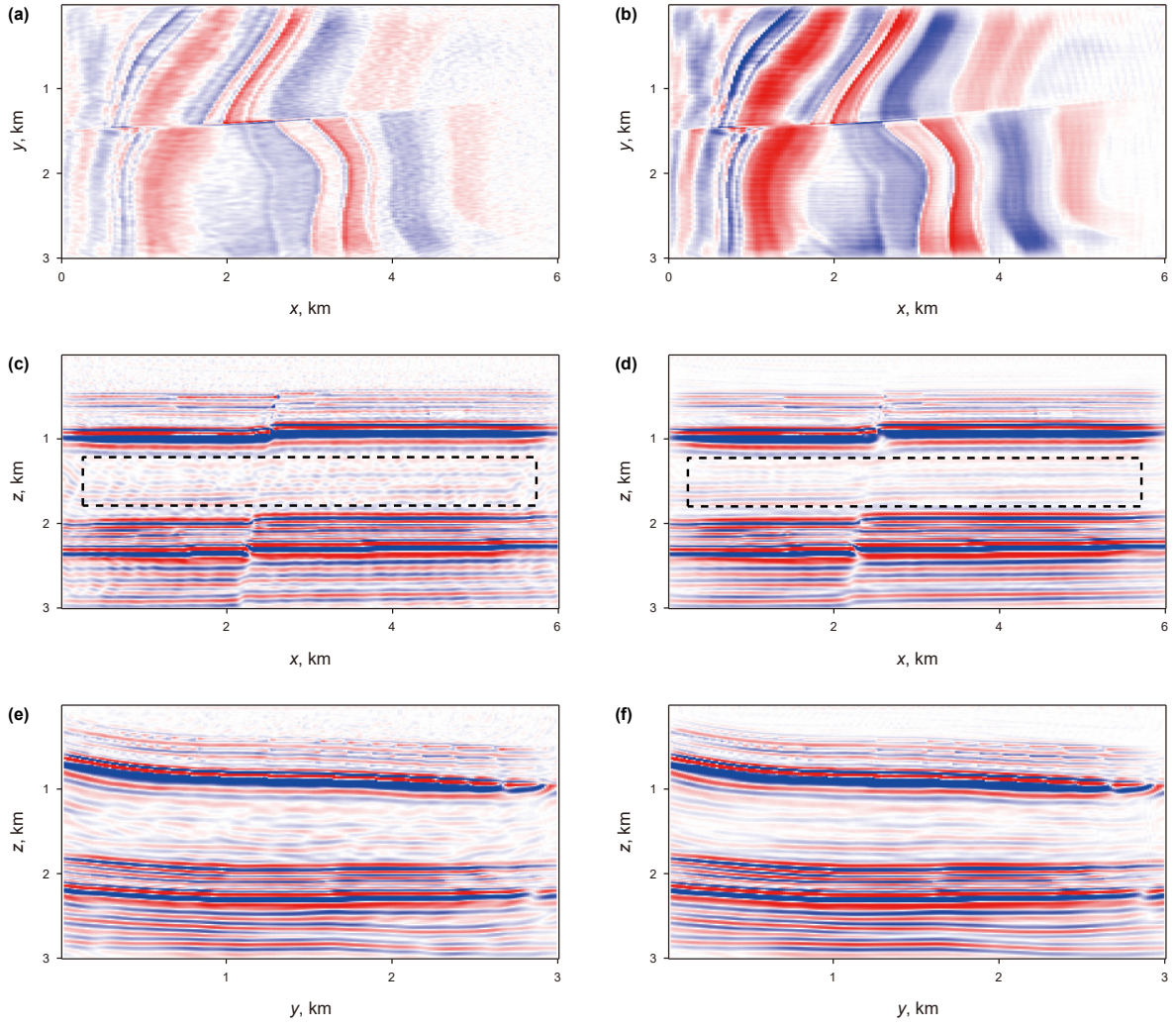

Fig. 15. The RTM images including the **(a)** *x*-*y*, **(c)** *x*-*z*, and **(e)** *y*-*z* slices using the input sparse and irregular data and the associated **(b)** *x*-*y*, **(d)** *x*-*z*, and **(f)** *y*-*z* slices using the regularized data.

3.2. Application to field data set

To demonstrate the method's capability in handling complex seismic events, we then applied it to a land dataset. The data set is indexed by the source coordinate (2D vector), the receiver coordinate (2D vector), and recording time. The original geometry is designed to have a receiver spacing of 140 m in crossline direction, and 20 m in inline direction, a source spacing of 120 m in inline direction, and 20 m in crossline direction. However, the raw data are sparsely acquired due to obstacles such as rivers and

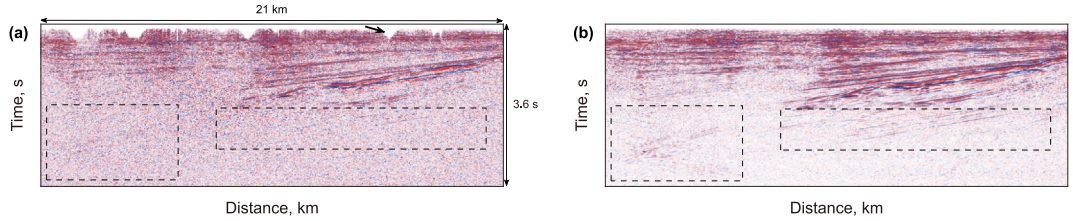

Fig. 16. One example of the stacked images **(a)** using the input seismic data and **(b)** the anti-aliasing ALFT regularized data.

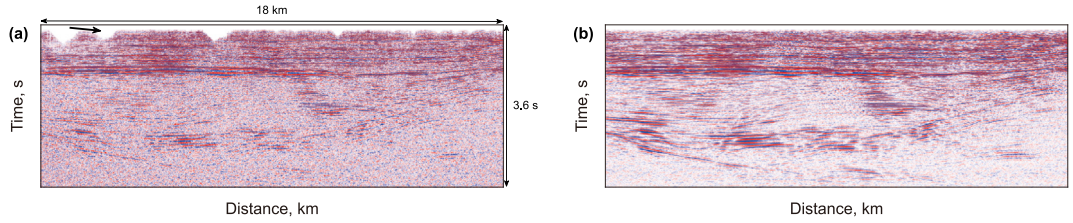

Fig. 17. Another example of the stacked images **(a)** using the input seismic data and **(b)** the anti-aliasing ALFT regularized data.

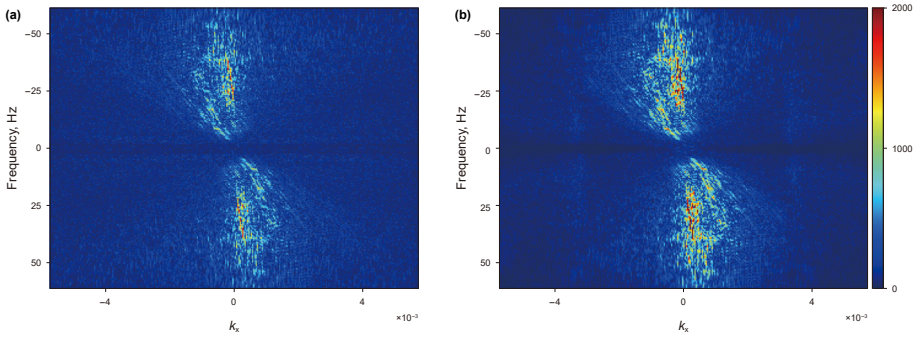

Fig. 18. The $f-k$ spectrum of **(a)** the stacked image in Fig. 16(a) and **(b)** the image in Fig. 16(b).

villages. The recording time is 6.0 s with 2 ms time-sampling interval. The proposed method is applied on vector source and receiver inline direction with one loop over receiver crossline direction, and the regularization grid is same with the original designed one.

We then applied NMO stacking to both the input data and the regularized data. Two stacked profiles are presented in Figs. 16 and 17 for comparison. It is evident that the quality of the stacked image after regularization is significantly improved regarding signal-to-noise ratio and event coherency, particularly the areas marked by dashed black rectangles. Besides, the acquisition holes pointed by the black arrows in Figs. 16(a) and 17(a) are reasonably filled after regularization. To further demonstrate the image quality improvement, we compute the $f-k$ spectra of the two images in Fig. 16(a) and (b), as depicted in Fig. 18(a) and (b), respectively. The comparison in Fig. 18 demonstrates that the spectrum after regularization has more focused energy and reduced high-wavenumber noise.

4. Discussion

The presence of low-velocity near-surface layers can lead to strong and low-traveling arrivals that obscure the primary reflections. Such arrivals are typically severely aliased even for the modern 3D seismic survey, and thus difficult to suppress due to inadequate spatial sampling. The proposed method can also be applied to effectively suppress this near-surface noise by reconstructing the spectrum free of aliasing and leakage and using a noise-removal window in $f-k$ domain.

Considering the seismic events are usually smoothly varying and piecewise linear, we operate the data reconstruction in many narrow temporal and spatial windows. For complex seismic data with rough topography, we need more iterations to reconstruct the spectrum because the complex seismic events on a frequency slice in the $f-k$ domain are not points-like; in this case, more traces are also required to well recover the missing traces.

Extending this method into 5D regularization might have a better performance than 4D version when dealing with input data that exhibits severe aliasing across all spatial dimensions, but much more memory and computational cost are required. Given the limitations of available GPU memory, we have designed this method to operate in 4D, which strikes a balance between memory consumption and result quality.

5. Conclusion

We proposed an anti-aliasing ALFT method using cube removal. This method can effectively regularize the combination of irregular sampling and aliasing of high-dimensional seismic data. We used cube-removal strategy to accelerate the convergence of the ALFT, and further designed one CPU/GPU parallel computing architecture to dramatically improve the regularization efficiency. The numerical test on both synthetic and field datasets validates that our method can well regularize the complex seismic data and can

further improve the prestack seismic data processing.

CRediT authorship contribution statement

Lu Liu: Writing – original draft & editing, Software, Validation, Methodology. **Sindi Ghada:** Investigation, Validation. **Fu-Hao Qin:** Project administration, Methodology. **Youngseo Kim:** Software, Validation. **Vladimir Aleksic:** Software, Validation. **Hong-Wei Liu:** Investigation.

Declaration of competing interest

The authors declare that they have no known competing financial interests or personal relationships that could have appeared to influence the work reported in this paper.

Acknowledgments

We appreciate the helpful discussions and comments of our colleagues Yi He, Yu-Jin Liu, Yue Ma, and Yi Luo. We also thank three anonymous reviewers for their useful suggestions.

References

Almutlaq, M.H., Margrave, G.F., 2010. Tutorial: AVO inversion. CREWES report 22, 1–23.
Abma, R., Kabir, N., 2006. 3D interpolation of irregular data with a POCS algorithm. Geophysics 71 (6), E91–E97. https://doi.org/10.1190/1.2356088.
Chemingui, N., 1999. Imaging Irregularly Sampled 3D Prestacked Data. Ph.D. thesis. Stanford University.
Crawley, S.E., 2001. Seismic Trace Interpolation with Nonstationary Prediction-Error Filters. Ph.D. thesis. Stanford University.
Duijndam, A.J.W., Schonewille, M.A., Hindriks, C.O.H., 1999. Reconstruction of band-limited signals, irregularly sampled along one spatial direction. Geophysics 64, 524–538. https://doi.org/10.1190/1.1444559.
Ebrahim, G., Liao, W., Lamoureux, M.P., 2018. Antileakage least-squares spectral analysis for seismic data regularization and random noise attenuation. Geophysics 83 (3), V157–V170. https://doi.org/10.1190/geo2017-0284.1.
Etgen, J., Gray, S.H., Zhang, Y., 2009. An overview of depth imaging in exploration geophysics. Geophysics 74 (6), WCA5–WCA17. https://doi.org/10.1190/1.3223188.
Fang, W.Q., Fu, L.H., Wu, M.Y., et al., 2023. Irregularly sampled seismic data interpolation with self-supervised learning. Geophysics 88 (3), V175–V185. https://doi.org/10.1190/geo2022-0586.1.
Hindriks, K., Duijndam, A.J.W., 2000. Reconstruction of 3D seismic signals irregularly sampled along two spatial coordinates. Geophysics 65, 253–263. https://doi.org/10.1190/1.1444716.
Jin, S., 2010. 5D seismic data regularization by a damped least-norm Fourier inversion. Geophysics 75 (6), WB103–WB111. https://doi.org/10.1190/1.3505002.
Liu, B., Sacchi, M.D., 2004. Minimum weighted norm interpolation of seismic records. Geophysics 69, 1560–1568. https://doi.org/10.1190/1.1836829.
Liu, L., Ding, R.W., Liu, H.W., et al., 2015. 3D hybrid-domain full waveform inversion on GPU. Comput. Geosci. 83, 27–36. https://doi.org/10.1016/j.cageo.2015.06.017.
Liu, L., Wu, Y., Guo, B.W., et al., 2018. Near-surface velocity estimation using source-domain full traveltime inversion and early-arrival waveform inversion. Geophysics 83 (4), R335–R344. https://doi.org/10.1190/GEO2017-0712.1.
Liu, L., 2019. Improving seismic image using the common-horizon panel. Geophysics 84 (5), S449–S458. https://doi.org/10.1190/GEO2018-0656.1.
Nemeth, T., Wu, C.J., Schuster, G.T., 1999. Least-squares migration of incomplete reflection data. Geophysics 64, 208–221. https://doi.org/10.1190/1.1444517.
NVIDIA Corporation, 2022. Nvcomp, a library for fast lossless compression/decompression on the GPU. https://github.com/NVIDIA/nvcomp.
Pawelec, I., Sava, P., Wakin, M., 2019. Wavefield reconstruction using wavelet transform. SEG Technical Program Expanded Abstracts, pp. 147–151.
Qin, F., Burnstad, R.M., Leger, P.C., 2012. An effective f-k domain random noise suppression technique applied to a land data set. 82th Annual International Meeting. SEG, Expanded Abstracts 1–5. https://doi.org/10.1190/segam2012-0964.1.
Qin, F., Leger, P.C., Ren, J.X., et al., 2018. A robust implementation and application of anti-leakage Fourier transform interpolation. Lead. Edge 37 (7), 538–543. https://doi.org/10.1190/tle37070538.1.
Schonewille, M., Andreas, K., Alan, V., 2009. Anti-alias anti-leakage Fourier transform. 79th Annual International Meeting, SEG Expanded Abstracts 3249–3253. https://doi.org/10.1190/1.3255533.
Spitz, S., 1991. Seismic trace interpolation in the f-x domain. Geophysics 56, 785–794. https://doi.org/10.1190/1.1443096.
Trad, D.O., Ulrych, T.J., Sacchi, M.D., 2002. Accurate interpolation with high-resolution time-variant Radon transforms. Geophysics 67 (2), 644–656. https://doi.org/10.1190/1.1468626.
Verschuur, D.J., Berkhout, A.J., Wapenaar, C.P.A., 1992. Adaptive surface-related multiple elimination. Geophysics 57, 1166–1177. https://doi.org/10.1190/1.1443330.
Verma, S., Guo, S., Marfurt, K.J., 2016. Data conditioning of legacy seismic using migration-driven 5D interpolation. Interpretation 4 (2), SG31–SG40. https://doi.org/10.1190/INT-2015-0157.1.
Wang, B., Zhang, N., Lu, W., 2019. Deep-learning-based seismic data interpolation: a preliminary result. Geophysics 84 (1), V11–V20. https://doi.org/10.1190/geo2017-0495.1.
Wang, Y., Lu, W., Li, Y., 2023. A self-adaptive anti-aliasing framework for seismic data interpolation. IEEE Trans. Geosci. Rem. Sens. 61. https://doi.org/10.1109/TGRS.2023.3272644.
Whiteside, W., Guo, M., Sun, J., et al., 2014. 5D data regularization using enhanced antileakage Fourier transform. 84th Annual International Meeting, SEG ExpandedAbstracts 3616–3620. https://doi.org/10.1190/segam2014-0724.1.
Xu, S., Zhang, Y., Pham, D., Lambare, G., 2005. Antileakage Fourier transform for seismic data regularization. Geophysics 70 (4), V87–V95. https://doi.org/10.1190/1.1993713.
Xu, S., Zhang, Y., Lambaré, G., 2010. Antileakage Fourier transform for seismic data regularization in higher dimensions. Geophysics 75 (6), WB113–WB120. https://doi.org/10.1190/1.3507248.
Yang, H., Li, J., Gan, L., et al., 2017. Fast antialiasing Fourier inversion for 5D seismic data regularization. SEG Technical Program Expanded Abstracts, pp. 4317–4321.
Zhang, H., Yang, X., Ma, J., 2020. Can learning from natural image denoising be used for seismic data interpolation. Geophysics 85 (4), WA115–WA136. https://doi.org/10.1190/geo2019-0243.1.
Zwartjes, P.M., Sacchi, M.D., 2007. Fourier reconstruction of nonuniformly sampled, aliased seismic data. Geophysics 72 (1), V21–V32. https://doi.org/10.1190/1.2399442.
Zwartjes, P.M., Gisolf, A., 2007. Fourier reconstruction with sparse inversion. Geophys. Prospect. 55 (2), 199–221. https://doi.org/10.1111/j.1365-2478.2006.00580.x.